Rev.Adv.Mater.Sci. 19 (2009) 78-92

MICROSTRUCTURAL MODELING OF NANOIDENTATIONAL POLYCRSYTALLINE GOLD WITH RANDOM HIGH ANGLE GRAIN-BOUNDARIES

Jeong Beom Ma and M.A. Zikry

Department of Mechanical and Aerospace Engineering, North Carolina State University, Raleigh, NC 27695-7910, USA

Received: November 22, 2008

Abstract. A hierarchical computational scheme that links molecular dynamic (MD) simulations to specialized finite-element (FE) microstructurally-based techniques has been used to predict how nanoindentation affects behavior in crystalline gold polycrystals aggregates with random high angle GBs. Displacement profiles from MD simulations of nanoindentation were used to obtain scaling relations, which are based on indented depths, grain-sizes, and grain aggregate distributions. These scaling relations are then used in a microstructurally based finite-element (FE) formulation that accounts for dislocation density evolution, plastic strains, crystalline structures, grain-sizes, and grain-boundary (GB) Effects. This computational methodology can be used to ascertain inelastic effects pertaining to nanoindentation, such as shear-slip distribution, pressure accumulation, and dislocation density and slip rate activation and evolution.

1. INTRODUCTION

Reliable nanoindentation measurements of material properties of nanocrystalline materials have been severely hampered by an inability to account for different physical mechanisms, such as grain-boundary (GB) effects, dislocation activities, and GB sliding that span different scales in ductile materials. An accurate understanding of nanoindentation is critical for reliable estimates of material properties for nanocrystalline aggregates. Inelastic behavior is difficult to characterize by nanoindentation due to localized dislocation activities over small volumes that can be dominated by a large fraction of GB surfaces (see, for example [1]). Furthermore, crystalline aggregates, which can be comprised of a collection of nanograins, can approach micro scales. Hence, the transition from the nano to the micro level behavior needs to be better understood and accurately predicted, suchthat indentation can be used to accurately predict material behavior at different scales.

The accurate measurement of the hardness of bulk and thin film crystalline materials, such as gold and copper, is critical due to the utility of these crystalline materials as coatings and conductors for semiconductor, microelectronic, and biomedical applications. Gane and Bowden [2] used a scanning electron microscope (SEM) and microindentation to determine the microstrength and microdeformation of gold, copper, and aluminum crystals. Atomic force microscopy (AFM) was used to investigate the hardness of gold thin films by applying the projected area calibration [3]. Indentation was used to determine the hardness of several materials including gold single crystals [4], and it was determined that hardness decreased with increasing depth irrespective of increasing or decreasing strain gradients. Smith and Zheng [5] investigated glass, gold, and single crystal silicon at room temperature and at 200 °C

Corresponding author: M.A. Zikry, e-mail: zikry@ncsu.edu

by using a depth sensing indentation instrument, and they concluded that the hardness value decreased with increases in temperature. Measurements from interfacial force microscope (IFM) have also been used in conjunction with nanoindentation. Michalske and Houston [6] used IFM to investigate the nano-scale elastic and plastic response of gold single crystal (111) surfaces by using controlled-probe contacts with different radii. They found that the stress at the plastic threshold increases with decreasing probe-tip radius. Kiely and Houston [7] extended these experiments to (110) and (001) surfaces of gold single crystals, and determined the elastic indentation modulus variation for different surfaces. Due to the effects of surface steps on the initiation of plastic yield, the mean stress at yield was found to be 30% to 45% lower at a step than in regions free of surface defects. It was observed in [8] that there are two distinct regimes of plastic deformation in gold films, which are distinguished by the magnitude of discontinuities in load relaxation. At lower stresses, relaxation occurs in small deviations from elastic behavior, while at the higher stresses they take the form of large load drops, often resulting in complete relaxation of the applied load. These major events create a relatively wide plastic zone that subsequently deepens more rapidly than it widens.

Schall and Brenner [9] used MD simulations, based on the embedded atom method (EAM), to show how small variations in the contact area during plastic indentation of Au (111) substrate under an applied in-plane stress can dramatically affect calculated hardness values. MD based techniques have been used to investigate gold surfaces and crystalline aggregates [3,10-12]. These investigations have generally provided an atomistic understanding of dislocation nucleation during displacement-controlled indentation on a passivated surface. An investigation by [12] has shown that for Au (111) surface, nucleation of partial dislocation loops occurs below the surface inside the indenter contact area. Furthermore, large-indenter force-displacement curves differ from that corresponding to the small indenter in one important respect, which is the absence of force drops during indentation, despite profuse dislocation activity. Large-scale MD simulations of gold nanocrystalline were undertaken by [13]. Their detailed analyses provided an understanding of how dislocations emit under an indenter, and how GB networks act as a sinks or as emitters of dislocations for a crystalline aggregate. Their simulations indicate that GBs act as efficient sinks for dislocation nucleation below the indenter, and that these sinks result in intergranular sliding. They also suggested that temporal and spatial scales of these modeling techniques precluded a detailed and accurate structural characterization of the simulated samples.

Miller, Shilkrot, and Curtin [14] adopted an atomic-scale model based on nonlinear finite element formulation to analyze the stress and strain induced in a very thin film during the nanoindentation. Their results indicated that the microscopic plastic deformation in thin films is due to the instability of its crystalline structure, and that the magnitude of the nanohardness varies with the maximum indentation depth and the geometry of the indenter. FE modeling and MD simulations were used by [15] to model the nanoindentation of aluminum on the silicon substrate. They concluded that their FE analyses have limited utility in rationalizing nanoindentation experiments in which discrete discontinuities are dominant, and that MD simulations can be used to simulate experimental observations related to defect nucleation. Multiscale quasicontinuum models of plasticity developed by [16] were used to elucidate the mechanisms of dislocation nucleation and interaction, and to illustrate how such information can be imported into explicit models of dislocation dynamics.

It is well understood that GB structure, orientation, and distributions are microstructural features that characterize the initiation and evolution of deformation and failure modes in crystalline metals, alloys, and intermetallics. As noted by [4,13,17,18], one of the major challenges is determining how dislocation density nucleation, emission, transmission, and absorption within GB regions affect overall inelastic behavior for crystalline materials subjected to nanoindentation. Furthermore, TEM investigations by [19] found an unusual microstructure, which contains vacancy-type point defect clusters of extraordinary high density near GB regions in gold aggregates. These defect clusters were produced in heavily deformed regions without dislocation motion. They suggested that the instability of crystalline state under tremendously high internal stress level is a key factor for the mechanism of dislocation free plastic deformation near GB regions.

Therefore, the physical scale on which to investigate different dislocation mechanisms involves different spatial and temporal levels that span the atomistic to the continuum levels. Atomistic methods are best suited for predictions related to defect nucleation, while microstructural and continuum-based

methods are best suited for how defects evolve beyond the nucleation threshold stage and how several dislocations evolve to a population density. Atomistic-based methods, due to spatial and temporal limitations, can be used to predict and model how phenomena, such as the initiation of GB sliding and the initiation of dislocations and other defects, but other methods need to be used beyond the nucleation stage associated with defect formation. Furthermore, it is also evident, that microstructural effects, such as collective grain activities and GB effects that are near the indented surface play a critical role in the overall behavior.

Therefore, the primary purpose of this study is to be able to understand and predict how dislocation densities and inelastic deformation modes evolve beyond the defect nucleation stage. In earlier investigations by the authors [20,29], a hierarchical computational model that spans the nano to the micro scales was developed and validated to investigate gold aggregates with cube orientations and random low-angle GBs. Displacement profiles, which can be obtained from MD simulations of nanoindentation, were used with specialized microstructural-based FE formulations to track the evolution of dislocation densities and inhomogeneous deformation modes in crystalline aggregates with different grain-sizes and GB orientations. An inelastic dislocation density based multiple-slip crystalline constitutive formulation was used, in conjunction with the hierarchical computational model, to obtain accurate predictions of local material mechanisms that control and affect inhomogeneous deformation modes in f.c.c. polycrystalline aggregates. In this paper, we will extend that formulation to account for a polycrystalline aggregates random high-angle GB distributions. This will be complement of the previous investigations, and it will delineate how random high angle GB orientations and distributions affect nanoindentation and dislocation density evolution. This paper is organized as follows: the multiple-slip crystalline plasticity, the coupled dislocation density evolution equations, and the microstructurally-based finite-element method are presented in Sections 2-3, the hierarchical scheme that links MD simulations with the FEM is presented in Section 4, the grain-boundary interaction mechanism is described in Section 5, the experimental validation of the computational approach and the results are given in Section 6, and a summary of the salient results are presented in Section 7.

2. MULTIPLE-SLIP DISLOCATION DENSITY BASED CRYSTAL PLASTICITY FORMULATION

An outline of the constitutive formulations for the rate-dependent multiple-slip crystal plasticity, which is coupled to the evolutionary equations for the dislocation densities, will be outlined here. A detailed presentation is given by Zikry and Kao [21].

It is assumed that the total deformation-rate tensor, D_{ij}, and the total spin tensor, W_{ij}, can be then additively decomposed into elastic and plastic components as

$$D_{ij} = D^{*}_{ij} + D^{P}_{ij}, \qquad W_{ij} = W^{*}_{ij} + W^{P}_{ij}, \tag{1a-b}$$

in which W_{ij} includes the rigid body spin. The inelastic parts are defined in terms of the crystallographic slip rates as

$$D^{p}_{ij} = P^{(\alpha)}_{ij}\dot{\gamma}^{(\alpha)}, \qquad W^{p}_{ij} = \omega^{(\alpha)}_{ij}\dot{\gamma}^{(\alpha)}, \tag{2a-b}$$

where $\dot{\gamma}_{ij}$ is summed over all slip systems, and P_{ij} and $\omega^{(\alpha)}_{ij}$ are second-order tensors, and are defined in terms of the unit normals to the slip planes and the unit slip vectors to the slip directions.

For rate-dependent inelastic materials, the constitutive description on each slip system can be characterized by a power law relation

$$\dot{\gamma}^{(\alpha)} = \dot{\gamma}^{(\alpha)}_{ref}\left[\frac{\tau^{(\alpha)}}{\tau^{(\alpha)}_{ref}}\right]\left[\frac{|\,\tau^{(\alpha)}\,|}{\tau^{(\alpha)}_{ref}}\right]^{\left(\frac{1}{m}\right)-1} \quad no\ sum\ on\ \alpha, \tag{3}$$

where $\dot{\gamma}^{(\alpha)}_{ref}$ is the reference shear strain rate which corresponds to a reference shear stress, $\tau^{(\alpha)}_{ref}$ and m is the rate sensitivity parameter. The reference stress that is used here is a modification of widely used classical forms that relate the reference stress to a square-root dependence on the dislocation density as

$$\tau^{(\alpha)}_{ref} = \tau^{(\alpha)}_{y} + Gb\sum_{\xi=1}^{12} a_{\xi}\sqrt{\rho^{(\xi)}_{im}}, \tag{4}$$

where G is the shear modulus, b is the magnitude of the Burgers vector, $\tau^{(\alpha)}_{y}$ is the static yield stress, and the coefficients, a_{ξ}, and ξ are interaction coefficients, and generally have a magnitude of unity.

3. EVOLUTIONARY EQUATIONS FOR THE MOBILE AND IMMOBILE DISLOCATION DENSITIES

The total dislocation density is assumed to be additively decomposed into a mobile dislocation density, $\rho_m^{(\alpha)}$, and an immobile dislocation density, $\rho_{im}^{(\alpha)}$, as

$$\rho^{(\alpha)} = \rho_m^{(\alpha)} + \rho_{im}^{(\alpha)}. \tag{5}$$

It is assumed that during an increment of strain, both dislocation density rates are generated and annihilated. The balance between dislocation generation and annihilation is the basis for the evolution of mobile and immobile dislocation densities as a function of strain. Based on these arguments, it can be shown (see [22]) that the coupled set of nonlinear evolutionary equations of mobile and immobile dislocation densities can then be given by

$$\frac{d\rho_m^{(\alpha)}}{dt} = \dot{\gamma}^{(\alpha)}\left[\frac{g_{sour}}{b^2}\left(\frac{\rho_{im}^{(\alpha)}}{\rho_m^{(\alpha)}}\right) - \frac{g_{minter}}{b^2}\exp\left(-\frac{H}{kT}\right) - \frac{g_{immob}}{b}\sqrt{\rho_{im}^{(\alpha)}}\right], \tag{6}$$

$$\frac{d\rho_{im}^{(\alpha)}}{dt} = \dot{\gamma}^{(\alpha)}\left[\frac{g_{minter}}{b^2}\exp\left(-\frac{H}{kT}\right) + \frac{g_{immob}}{b}\sqrt{\rho_{im}^{(\alpha)}} - g_{recov}\exp\left(-\frac{H}{kT}\right)\rho_{im}^{(\alpha)}\right], \tag{7}$$

where g_{sour} is a coefficient pertaining to an increase in the mobile dislocation density due to dislocation sources, g_{minter} is a coefficient related to the trapping of mobile dislocations due to forest intersections, cross-slip around obstacles, or dislocation interactions, g_{recov} is a coefficient related to the rearrangement and annihilation of immobile dislocations, g_{immob} is a coefficient related to the immobilization of mobile dislocations, H is the activation enthalpy, and k is Boltzmann's constant. As these evolutionary equations indicate, the dislocation activities related to recovery and trapping are coupled to thermal activation. The enthalpy, H, is determined by defining an exponential ratio of the current temperature to the reference temperature, following as a form of activation enthalpy for cross-slip which accounts the cross-slip effects. The four g coefficients are determined using two general conditions, pertaining to the evolution of dislocation densities in crystalline materials, have been used:

(i) that the mobile and immobile dislocation densities saturate at large strains;

(ii) that the relaxation of the mobile dislocation density to a quasi-steady state value occurs much faster than the variation of the immobile dislocation density.

Furthermore the total deformation rate tensor, and the plastic deformation rate tensor are needed to update the material stress state. The method used here is one developed by Zikry [23] for rate-dependent crystalline plasticity formulations. An implicit finite-element method is used to obtain the total deformation rate tensor. To overcome numerical instabilities associated with stiffness, a hybrid explicit-implicit method is used to obtain the plastic deformation rate tensor. This hybrid numerical scheme is also used to update the evolutionary equations for the mobile and immobile densities.

4. HIERARCHICAL MODELING OF NANOINDENTATION: LINKING AND SCALING OF MOLECULAR DYNAMIC SIMULATIONS WITH THE MICROSTRUCTURALLY BASED FINITE-ELEMENT FORMULATION

In this section, the methodology for linking MD simulations with the microstructurally based FEM formulation is briefly outlined. Details can be found in Ma *et al.* [20]

For the microstructural model, an aggregate with Euler angle orientations that do not exceed 30° for all the grains and GBs was used, such that it is representative of random high angle GBs. The material properties that were used in these models, are representative of pure gold [24], and are given in Table 1. It was assumed that all twelve slip systems for this f.c.c. aggregates were potentially active. Using the method outlined in [25], the saturated immobile dislocation density, $\overline{\rho}_{ims}$, was calculated as $1.0\cdot10^{16}$ m^{-2} and the saturated mobile dislocation density, $\overline{\rho}_{ims}$, was calculated as $4.3\cdot10^{13}$ m^{-2}. The initial mobile dislocation density of the grain bulk was chosen as 10^7 m^{-2}, and the initial immobile dislocation density was chosen as 10^{10} m^{-2}. These are values that are typical of f.c.c. crystalline aggregates. Using these values, the coefficient values and the enthalpy, needed for the evolution of

Table 1. Material properties for gold crystals.

Young's modulus 78 GPa	Yield stress 78 MPa
Poisson's ratio 0.35	Rate sensitivity factor 0.01
Reference strain rate 0.001/s	Critical strain rate 10^4/s
Burgers vector $3.0 \cdot 10^{10}$ m	Reference stress interaction coefficients
	a_i (i =1,12) 0.50

the immobile and mobile dislocation density equations (6-7), are calculated as $g_{miniter} = 2.013$, $g_{recov} = 4$, $g_{immob} = 0.02$, $g_{sour} = 2.76 \cdot 10^{-5}$, $H/k = 3.289 \cdot 10^3$ °K. (8)

From representative MD nanoindentation simulations, (see for example, [9] and [13]), which are based on a load-displacement input, we obtained different displacement profiles related to different contact depths and indentation surface profiles. These MD displacement profiles were obtained from the application of contact forces as a function of displacement. The predicted MD indentation depths (or applied displacements) were normalized by the specimen height, which would correspond to a normal strain. This normal strain, which is *scale invariant*, was then used to obtain displacement histories or indentation depths, as a function of the contact radius for the FE model. For the detailed description, see [29].

In this study, two different sized aggregates were used to investigate how inelastic deformation evolves at the microstructural scale for the high-angle distribution aggregates. The nodal displacements are applied on the indented surface, and the slope for loading and unloading paths are determined from [9]. The unloading slope is measured at the beginning of each step, which is consistent with experimental approaches. The slope in the unloaded region is approximately 20% higher than the slope in the loaded region. After a convergence analysis, 1455 quadrilateral elements were used for Model 1 and 2146 quadrilateral elements were used for Model 2.

As a virtual indenter for our FEM model, the displacement profiles for each node, in the contact region, for different indentation depths, were applied. Each node was displaced based on the strain that corresponds to the different indentation depths. At the beginning of the indentation, only one node is displaced and adjacent nodes are also displaced as the time step increases. Calculated axial distances between the center of the virtual indenter and the coordinate of each node are used for the displacement curve at each node. With this scheme the number of loaded nodes increases as the indentation depth increases.

5. GRAIN-BOUNDARY(GB) INTERFACIAL REGIONS AND INTERACTION MECHANISMS

It is well understood from numerous investigations pertaining to the experimental characterization of GB physical systems, such as intrinsic thermomechanical properties, operative crystallographic systems, and dislocation mechanisms that these all may be substantially different than those associated with the aggregate crystalline bulk response (see, for example, [32,34,35]). These studies further indicate that GB regions normally have inherently unique geometrical structures due to misorientations between adjacent grains that occur over distinct spatial widths and distributions.

As noted by [35], GB regions can be envisioned as highly localized transitional regions of finite widths with an atomic periodicity that is different than that of the contacting crystals. This transitional region can consist of defects, such as different dislocations, serrations, microfacets, and protrusions. Furthermore, at homologous temperatures (approximately at 40% of the melting temperature), GB regions can be strong obstacles to dislocation motion, and this can result in substantial increases in the overall flow response of polycrystalline aggregates in comparison with the response of monocrystalline structures. In addition, interfacial misorientations between grains can involve the translation and rotation of one crystalline lattice with respect to adjacent grains.

In this study, the orientation of each crystal is given by three Euler angles, φ_1, Φ, φ_2, and the orientation of the GB is given by a normal vector to the GB plane, $\tilde{n}_{gb}$. Therefore, these four degrees of freedom will be sufficiently representative for planar deformation.

There is a myriad of dislocation density interactions with GB interfaces, such as:

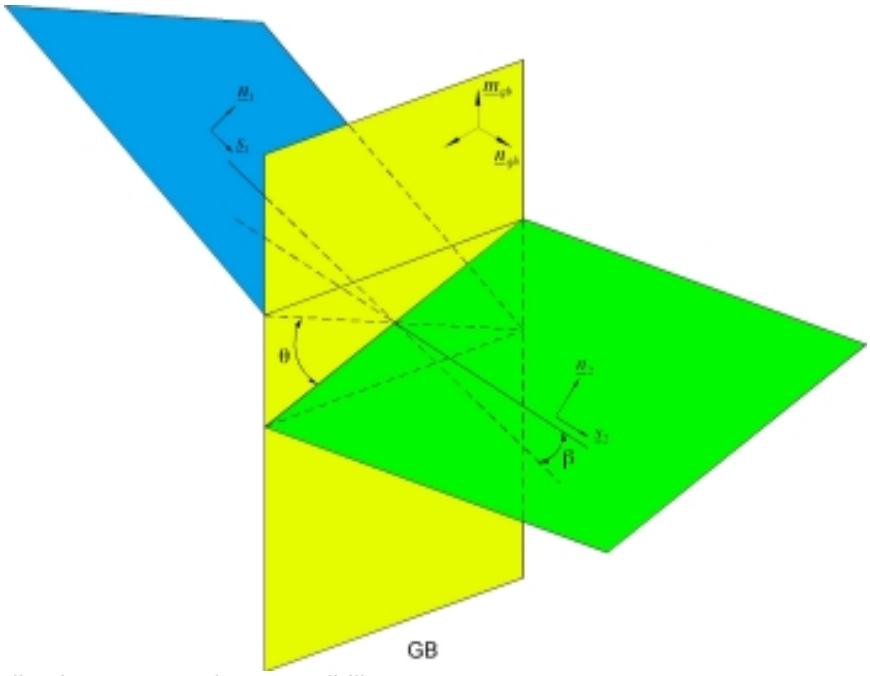

Fig 1. General slip plane geometric compatibility.

- GB absorption of lattice dislocations without dissociation into GB-dislocations (GBD) ([31,34]);
- Partial dislocation transmission from one grain to the adjacent grain with a residual GBD left in the GB region ([33,34]);
- Full dislocation transmission from one grain to the adjacent grain with no residual GBD left in the GB region ([33,34]).

We will focus on the following interactions:

- Full and partial dislocation density transmission from one grain to neighboring grains;
- Full and partial dislocation density transmission into GB and blockage at neighboring grains;
- Dislocation density impedance and potential pile-ups.

These kinematical scenarios provide a general methodology that can be used as a framework for GB interfacial mechanism and interactions.

Dislocation density transmission and impedance from one grain to neighboring grains across GB regions, will be determined through the following interrelated steps:

- A potential dislocation density envelope will be used to identify regions of high dislocation activities;
- Coordinate frame transformations will be performed with respect to the GB to identify the direction of the slipsystem associated with critical dislocation density systems;
- Conditions will be obtained for geometric compatibility to determine whether neighboring slipsystems are oriented for transmission or impedance through GB.

If transmission is possible, through the GB, a transformation factor will be calculated. Detailed description how to transform the dislocation density orientation and GB coordinate frame can be found in [30].

It is obvious that geometric compatibility affects to a larger degree dislocation density transmission. Previously, we mentioned that the most favorable configuration occurs when $\theta = 0$ and $\beta = 0$. (Fig. 1) This indicates complete transmission. Deviation from this configuration would represent a partial transmission through the interface. A transmission factor ζ, based on θ and β, will be defined as

$$\zeta = \cos\theta \cos\beta. \tag{9}$$

This will provide a measure of how much of the dislocation density penetrates through the GB and into neighboring grains.

6. RANDOM HIGH ANGLE GB EFFECTS ON NANOINDENTATION OF POLYCRYSTALLINE AGGREGATES

In J.B. MA and M.A. Zikry [29], we presented results for low angle GB misorientation distribution

for polycrystalline aggregates. We will investigate the nanoindentation of aggregates with high angle misorientations of grains and GBs, where the misorientations do not exceed 30°. We will also investigate how nanoindentation is affected by these high angle GBs. We will analyze the effects of grain and aggregate size and how GB strengths affect deformation modes induced by nanoindentation. The strength of the GB will be modified in the similar way as done by [30] where the initial GB static yield strength and modulus were assumed to three times higher than nearby grains.

6.1. Modeling of polycrystalline aggregates with high angle GBs

Two polycrystalline aggregates with average grain sizes of 0.003 mm and 0.0022 mm were investigated. It was assumed that the GB region is one-tenth of the grain diameter for both grain sizes. In this formulation, the mesh area corresponding to the GB region is modeled as a distinct region from the grain interior, and hence the dislocation density evolution and properties can be varied within the GB. All regions were randomly misoriented by Euler angles, φ_1, Φ, and φ_2, and its maximum misorientation angle is constrained by thirty degrees, such that it is representative of random high angle GB distribution. The same loading rates and properties that were used in [20] are used here. The schematic for the nanoindentation Model of the polycrystalline aggregates with the distinct GBs is provided in [20]. In the interfacial GB regions, the initial mobile and immobile dislocation densities were varied as a function of the random GB misorientation as

$$\rho_{imo}^{GB} = \rho_{imo}^{G} \times \kappa, \tag{10a}$$

$$\rho_{mo}^{GB} = \rho_{mo}^{G} / \kappa, \tag{10b}$$

where κ is 1.58^{θ}, θ is the maximum misorientation angle, ρ_{imo}^{GB} is the interfacial GB initial immobile dislocation density, ρ_{mo}^{GB} is the interfacial GB initial mobile dislocation density, ρ_{imo}^{G} is the bulk initial immobile dislocation density, and ρ_{mo}^{G} is the bulk initial mobile dislocation density. The initial immobile (ρ_{imo}^{G}) and mobile (ρ_{mo}^{G}) dislocation density values for bulk grain were given in [20]. And the initial immobile (ρ_{imo}^{GB}) and mobile (ρ_{mo}^{GB}) dislocation density values for GBs vary 10^{10}~10^{12} m^{-2} for immobile and 10^{5} ~ 10^{7} m^{-2} for mobile as in [27].

The following assumptions were also used:

- The initial GB static yield stress and modulus were assumed to be the same as the bulk grain;
- The GB dislocations are of the same type as the bulk lattice.

6.2. Grain size effects and slipsystem activities during local unloading

To investigate grain-size effects, different grain-sizes were investigated. Model 1 had grain-sizes of 0.003 mm and 15 grains, while Model 2 had grain-sizes of 0.0022 mm and 28 grains. The global stress-strain curves of these models at indentation depths of 9% and 12.8% are shown. As the compressive nominal strains increase, the nominal stress increases. Slipsystem activity changes of the stress-strain curve during the local unloading are shown in Table 2. Different slip systems were active before and after the load-drop in polycrystalline aggregates. For Model 1 at a normalized depth of 9% and 12.8%, slip system 4(C1 according to the Schmid and Boas notation, see [20] and Table III) was most active before and after the local load-drops. However, the most active slip systems varied for different slip systems before and after the load drop in Model 2. Based on this investigation, the smaller grain-sized model (Model 2) had the most slip system activity variation during the local unloading steps. This is due to lattice rotations and plastic strain accumulation and pressures in the indented grains, which have been experimentally observed by [6]. We also found that the load-drop during the indentation of polycrystalline aggregates affects the dislocation slip

Table 2. Slip system activity variation before and after the load drops during global loading (high angle GB misorientation).

Normalized Indented Depth	Before load drop	After load drop
9% Model 1	4	4
12.8% Model 1	4	4
9% Model 2	11	3
12.8% Model 2	3	10

Table 3. Slip systems numbering and corresponding slip planes and directions.

Slip system number	Slip plane unit normal $\tilde{n}$	Slip direction unit normal $\tilde{s}$	Schmid & Boas notation
1	$(1/\sqrt{3})(111)$	$(1/\sqrt{2})[\bar{1}01]$	B4
2	$(1/\sqrt{3})(111)$	$(1/\sqrt{2})[\bar{1}10]$	B5
3	$(1/\sqrt{3})(111)$	$(1/\sqrt{2})[0\bar{1}1]$	B2
4	$(1/\sqrt{3})(\bar{1}\ \bar{1}1)$	$(1/\sqrt{2})[011]$	C1
5	$(1/\sqrt{3})(\bar{1}\ \bar{1}1)$	$(1/\sqrt{2})[\bar{1}10]$	C5
6	$(1/\sqrt{3})(\bar{1}\ 11)$	$(1/\sqrt{2})[101]$	C3
7	$(1/\sqrt{3})(\bar{1}11)$	$(1/\sqrt{2})[101]$	A3
8	$(1/\sqrt{3})(\bar{1}11)$	$(1/\sqrt{2})[110]$	A6
9	$(1/\sqrt{3})(\bar{1}11)$	$(1/\sqrt{2})[0\bar{1}1]$	A2
10	$(1/\sqrt{3})(1\bar{1}1)$	$(1/\sqrt{2})[011]$	D1
11	$(1/\sqrt{3})(1\bar{1}1)$	$(1/\sqrt{2})[110]$	D6
12	$(1/\sqrt{3})(1\bar{1}1)$	$(1/\sqrt{2})[\bar{1}01]$	D4

system activities, and this was similar to predictions pertaining to the low angle GB models of [29].

6.3. Immobile dislocation density evolution, plastic strain, pressure response, effects of increased depths, and aggregate sizes: Model 1 and Model 2

The most active slip systems at the final loading step at different normalized depths were investigated to determine how the immobile dislocation densities on these systems evolve, and the summary is given in Table 4. By investigating material behavior at the final loading and unloading steps, we determined that slip system 4 was the most active slip system at the final loading step at an indentation of 9% indentation for Model 1. Immobile dislocation density evolved to $3.2{\cdot}10^{15}$ m^2, (32% of the saturation value). The total immobile dislocation density for all slip systems had evolved to $7.5{\cdot}10^{15}$ m^{-2}, which is 75% of the saturation value (Fig. 3). Hence, the immobile dislocation density of the most active slip system accounts for 42% of all immobile dislocation density activities. This may be due to the slip system activity impedance due to the highly misoriented distribution of Euler angles between grains and GBs. The immobile dislocation density at final global unloading of slip system 4 ($2.3{\cdot}10^{16}$ m^{-2}) and total immobile dislocation density ($5.7{\cdot}10^{16}$

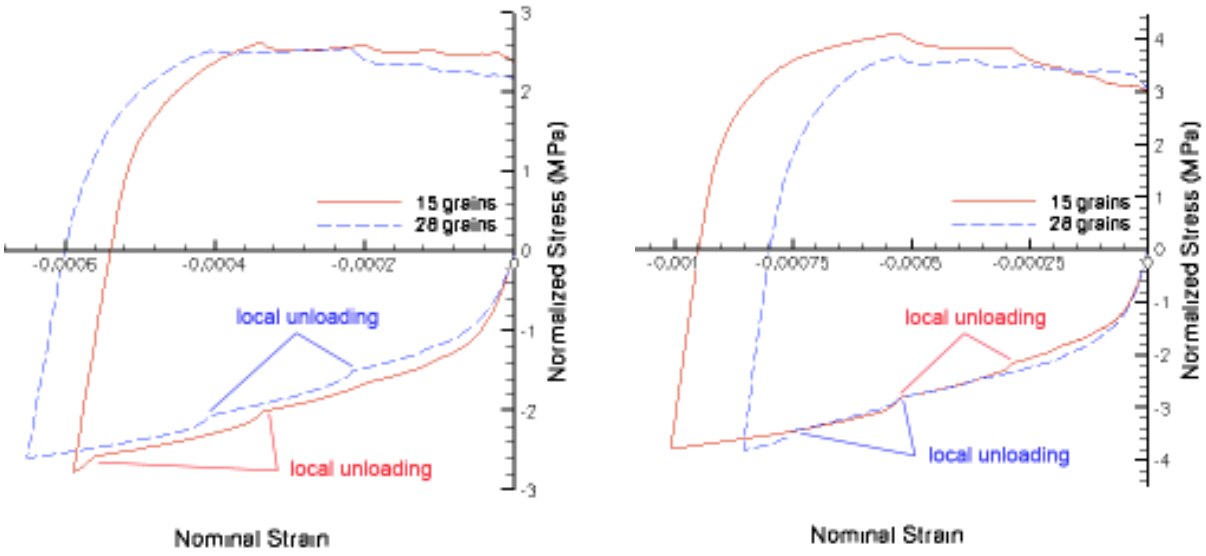

Fig 2. Stress-strain curves for gold polycrystalline aggregates with different normalized indented depths, aggregate sizes, and high angle misorientations (a) 9% and (b) 12.8%.

Table 4. List of most active slip systems at maximum normalized depths.

Normalized Indented Depth	Most active slip systems	Normalized Indented Depth	Most active slip systems
9% Model 1	4	9% Model 2	11
12.8% Model 1	5	12.8% Model 2	10

m^{-2}) at the same step are shown in Fig. 3. This indicates that more dislocation density activity evolved during unloading than during loading. After unloading, this system accounts for 40% of the total immobile dislocation density evolution. Similar to single crystals models [20], immobile dislocation density continues to evolve during the unloading step. The highly localized distribution of the immobile dislocation density was also evident at either side of the indenter for the most active slip system for both the final loading and unloading steps. This indicates that different slip systems are activated during unloading, and this is related to the residual strains due to inelastic activity.

The accumulated plastic strains and pressure distributions at the final loading and unloading step are shown in Fig. 3. Smaller plastic strains have accumulated (1.57) than the random low angle GB models (2.00) [29] in the regions corresponding to the highest immobile dislocation density areas at the final loading. The highest negative normalized pressures at the final loading step are in the same regions with a normalized value of -15.03.

We also indented model 1 to the normalized depth of 12.8% as shown in Fig. 4. At a normalized depth of 12.8%, slip system 5 had the highest immobile dislocation density evolution of $4.81 \cdot 10^{15}$ m^{-2} at final loading step, which is 48% of the saturation value. The total immobile dislocation density evolved to $1.23 \cdot 10^{16}$ m^{-2} (Fig. 4). At unloading, the most active slip system had an immobile dislocation density of $1.34 \cdot 10^{16}$ m^{-2}, and the total immobile dislocation density is $7.28 \cdot 10^{16}$ m^{-2} (Fig. 4). The portion of active systems at final loading is 39%. However, it decreases to 18.4% during the final unloading step. This indicates that the active slip systems have significantly increased during the unloading stages. Hence, as the normalized depth increases, and more grains are indented, the residual strains in the deformed grains result in more slip

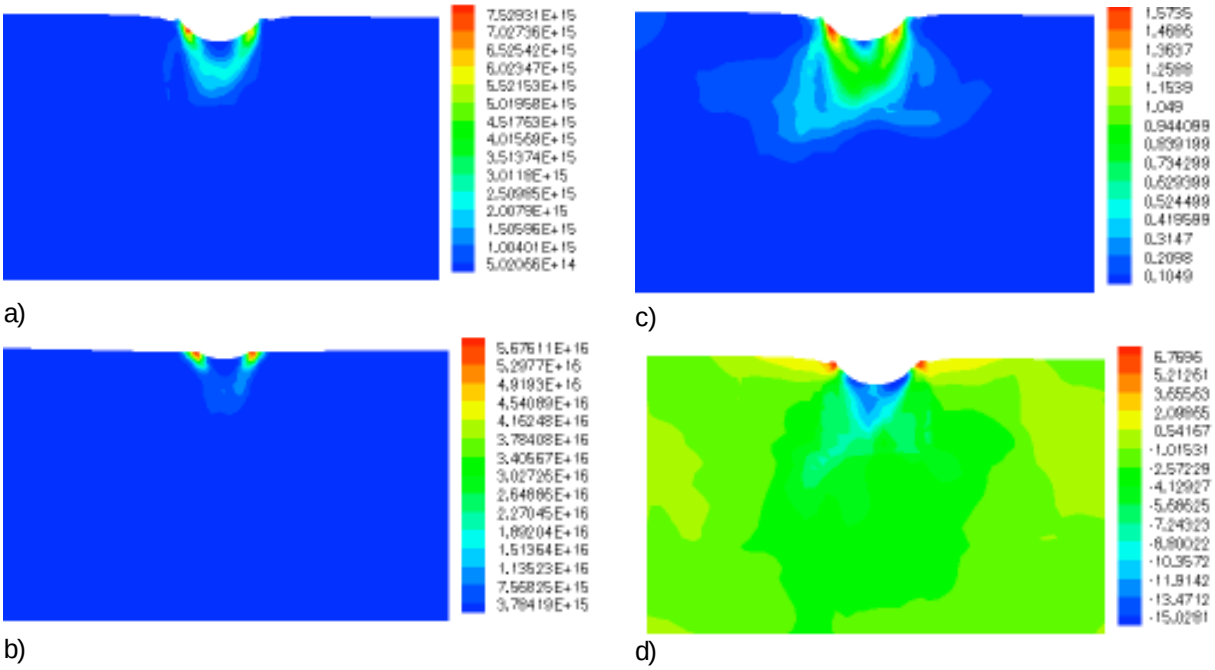

Fig. 3. Total Immobile dislocation density (a) at final loading step, (b) just before final unloading, (c) Plastic strain accumulation at final loading step and (d) normalized pressure at final loading step: Model 1 at 9% indentation.

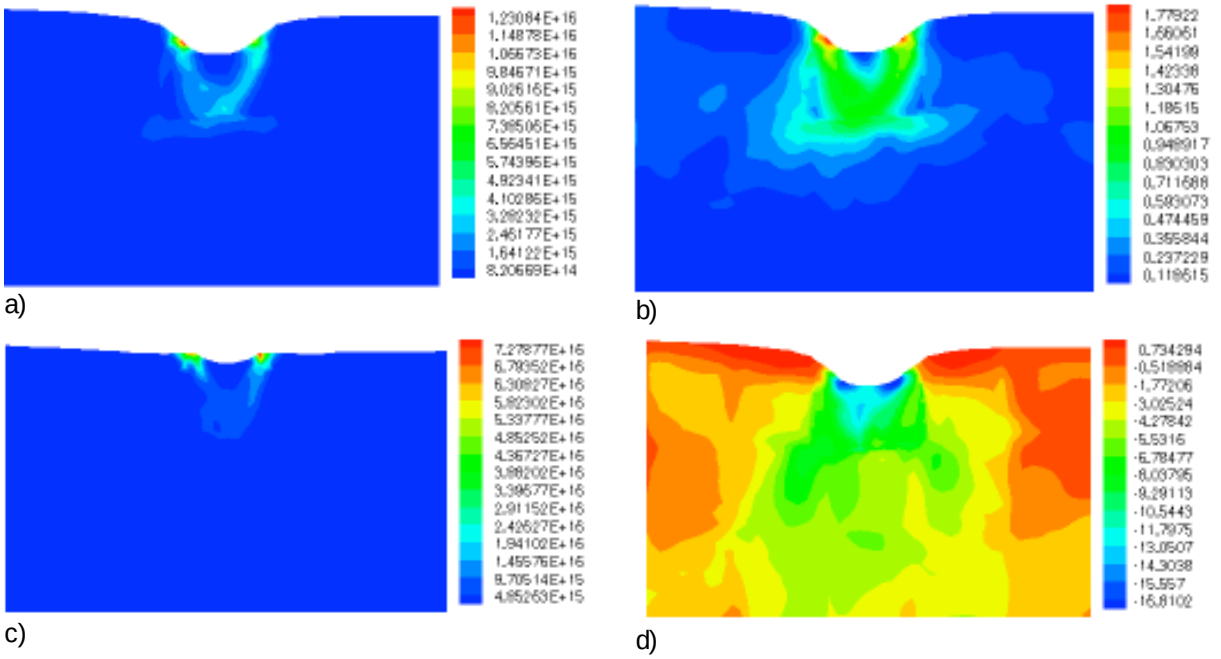

Fig 4. Total Immobile dislocation density (a) at final loading step, (b) just before final unloading, (c) Plastic strain accumulation at final loading step and (d) normalized pressure at final loading step: Model 1 at 12.8% indentation.

systems activation. This is consistent with experimental observations (see, for example, [15]), which indicate that dislocations and strains accumulate within the specimen after unloading. The accumulated plastic strains have also increased to approximately 13% (1.78) from the 9% indentation model at the final loading step. The pressures attain the highest negative normalized value of –16.8 at the maximum loading point (Fig. 4).

We investigated smaller grain-size (Model 2) for two normalized indentation depths. For 9% normalized indentation depth, slip system 11 was the most active at the final loading step. The immobile dislocation density is $6.34 \cdot 10^{15}$ m^{-2} (63% of the saturation value). At the final unloading stages, this immobile dislocation density had evolved to $3.85 \cdot 10^{16}$ m^{-2} for total immobile dislocation density. At 12.8% normalized indentation depth, the total immobile dislocation density had evolved to $2.38 \cdot 10^{16}$ m^{-2} at the final loading, and $1.72 \cdot 10^{17}$ m^{-2} at final unloading (Fig. 5). Both the accumulated plastic strains and pressures have continuously increased for this model (Fig. 6). The high immobile dislocation densities were accumulated at the regions, which had highest pressures during the loading and unloading stages.

6.4. Effects of high strength GBs on nanoindentaiton

In this section we investigated the results of the stronger GB models, which we assumed to have three times the initial GB static yield strength than the surrounding grain interiors for both grain aggregates. Model 3 has large grain-sizes (0.003 mm), and 9% indentation depth was applied. Slip system 1 was the most active slip system at the final loading step and had immobile dislocationdensity of $3.24 \cdot 10^{15}$ m^{-2} (32% of the saturation value). The total immobile dislocation density evolved to $8.71 \cdot 10^{15}$ m^{-2} at the final loading stage. At the final unloading, the most active slip system 1 had $2.09 \cdot 10^{16}$ m^{-2} and total immobile dislocation density had $6.52 \cdot 10^{16}$ m^{-2} (Fig. 7). At the final loading step, immobile dislocation density of the most active slip system accounts for 37% and at final unloading step, it accounts for 32% of total immobile dislocation dislocation evolution. This was less than that corresponding to Model 1.

For the smaller grain-sized aggregate (0.0022 mm, Model 4), the immobile dislocation density is $4.04 \cdot 10^{15}$ m^{-2}, (40% of saturation value) at the final loading step for most active slip system 3. The total immobile dislocation density was $9.24 \cdot 10^{15}$ m^{-2} at the final loading step. At the final unloading step,

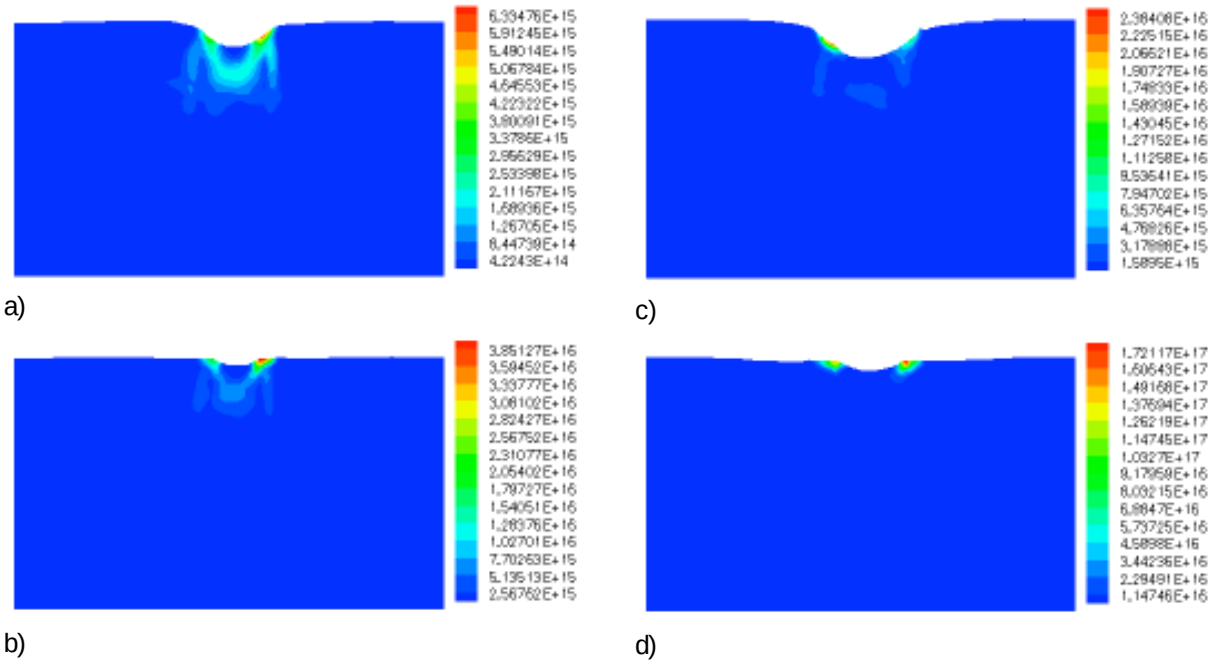

Fig 5. Total Immobile dislocation density (a) at final loading step, (b) just before final unloading - Model 2 at 9% indentation, (c) at final loading step, (d) just before final unloading - Model 2 at 12.8% indentation.

the dislocation density for system 3 had evolved to $2.0 \cdot 10^{16}$ m^{-2}. For the same step, the total immobile dislocation density is $4.66 \cdot 10^{16}$ m^{-2} (Fig. 7). Similar to model 3, model 4 showed more dislocation density evolution than model 2. Based on these results, the immobile dislocation density evolved more actively in models, which have stronger GB initial static yield strength than models that have same initial GB yield strength as the grain interiors.

We investigated regions under the indenter and adjacent GBs to determine the influences of indentation and their spatial and angular variation of im-

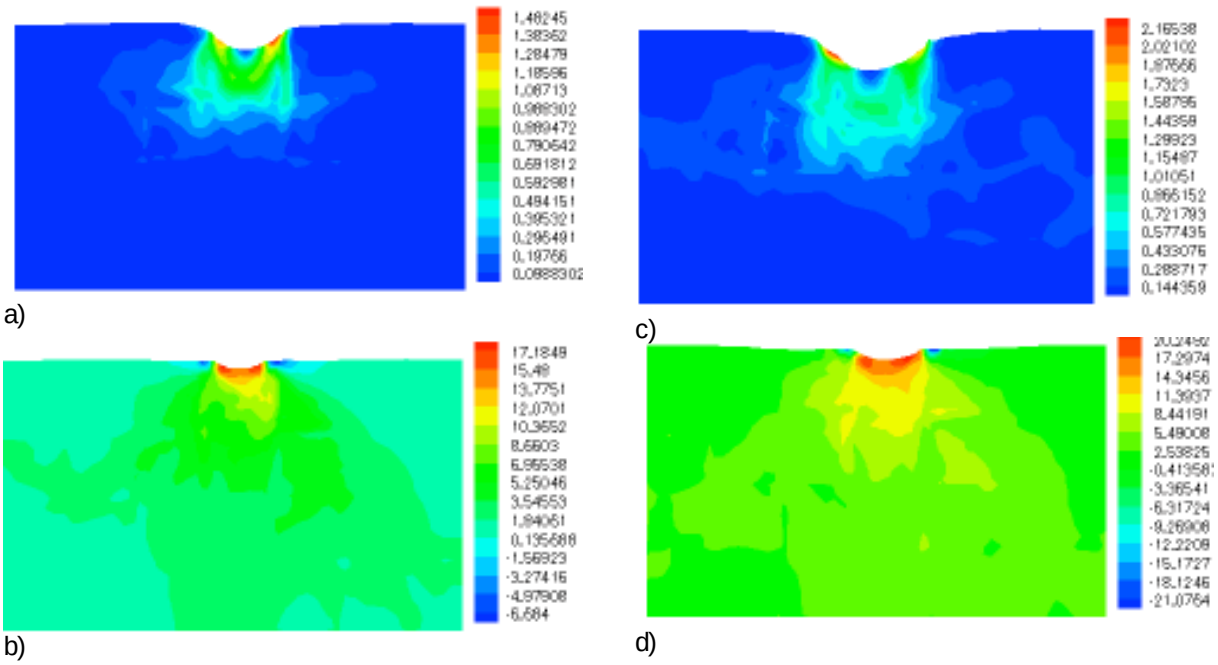

Fig 6. (a) Plastic strain accumulation at final loading step, (b) normalized pressure at just before final unloading – Model 2 at 9% indentation, (c) Plastic strain accumulation at final loading step, (d) normalized pressure at just before final unloading – Model 2 at 12.8% indentation.

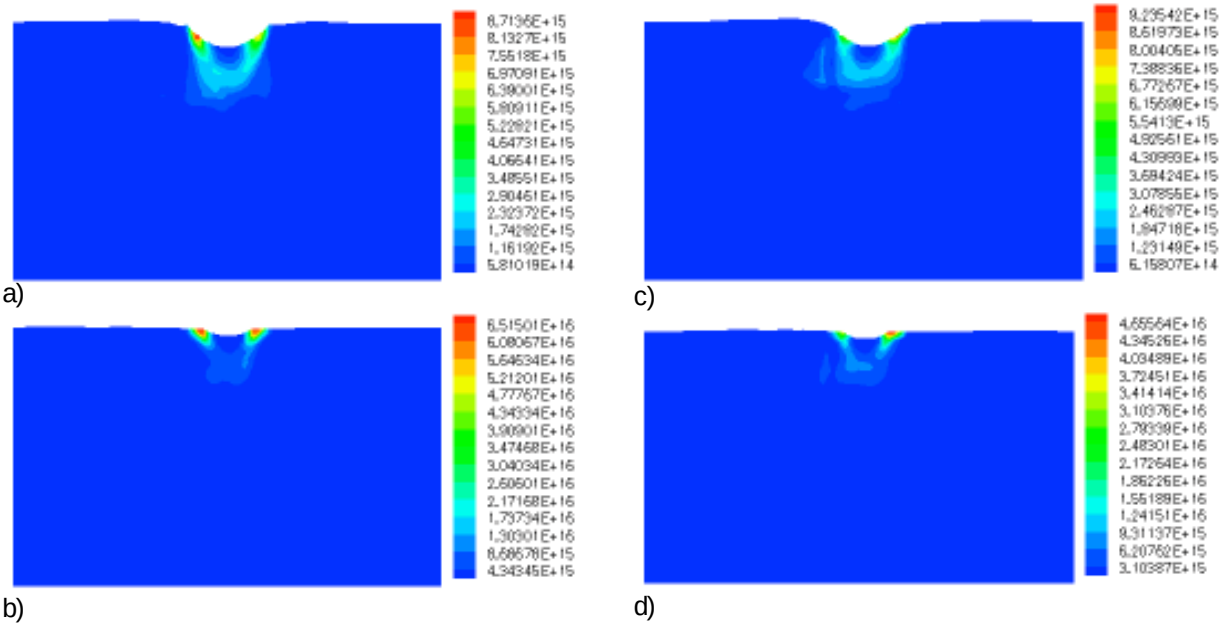

Fig 7. Total Immobile dislocation density, (a) at final loading step, (b) just before final unloading - Model 3 at 9% indentation, (c) at final loading step, (d) just before final unloading - Model 4 at 9% indentation.

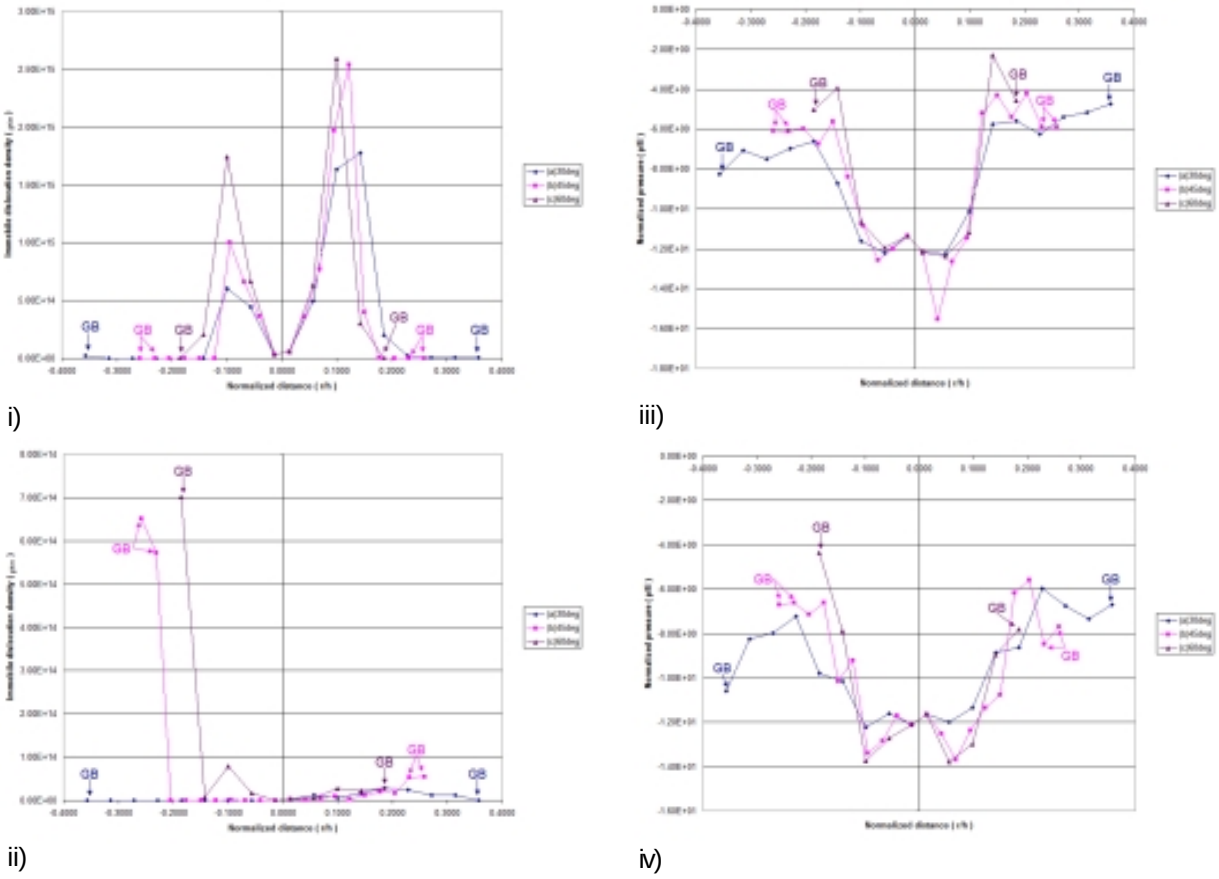

Fig 8. Immobile dislocation density distribution along the different angles with respect to loading axis at final loading – Model 1; (i) 9%, and (ii) 12.8%. Pressure distribution along the different angles with respect to loading axis at final loading – Model 1; (iii) 9%, and (iv) 12.8%. (a) ±30º (GB: r/h=0.3569), (b) ±45º (GB: *r*/*h*=0.2312 and 0.2584), (c) ±60º (GB: *r*/*h*=0.185).

mobile dislocation densities, plasticstrains, and pressures on that grain and GBs at critical locations. Fig. 8 shows the immobile dislocation density variation for Model 1 at different normalized indentation depths. The immobile dislocation density values varied along the angular directions, and they are highest under the indenter. However, at an indentation of 12.8%, the immobile dislocation density increased at the left side of the indenter near the specimen surface and at the GBs, which coincides with the increase of pressures and plastic strains at the same regions. The normalized pres-

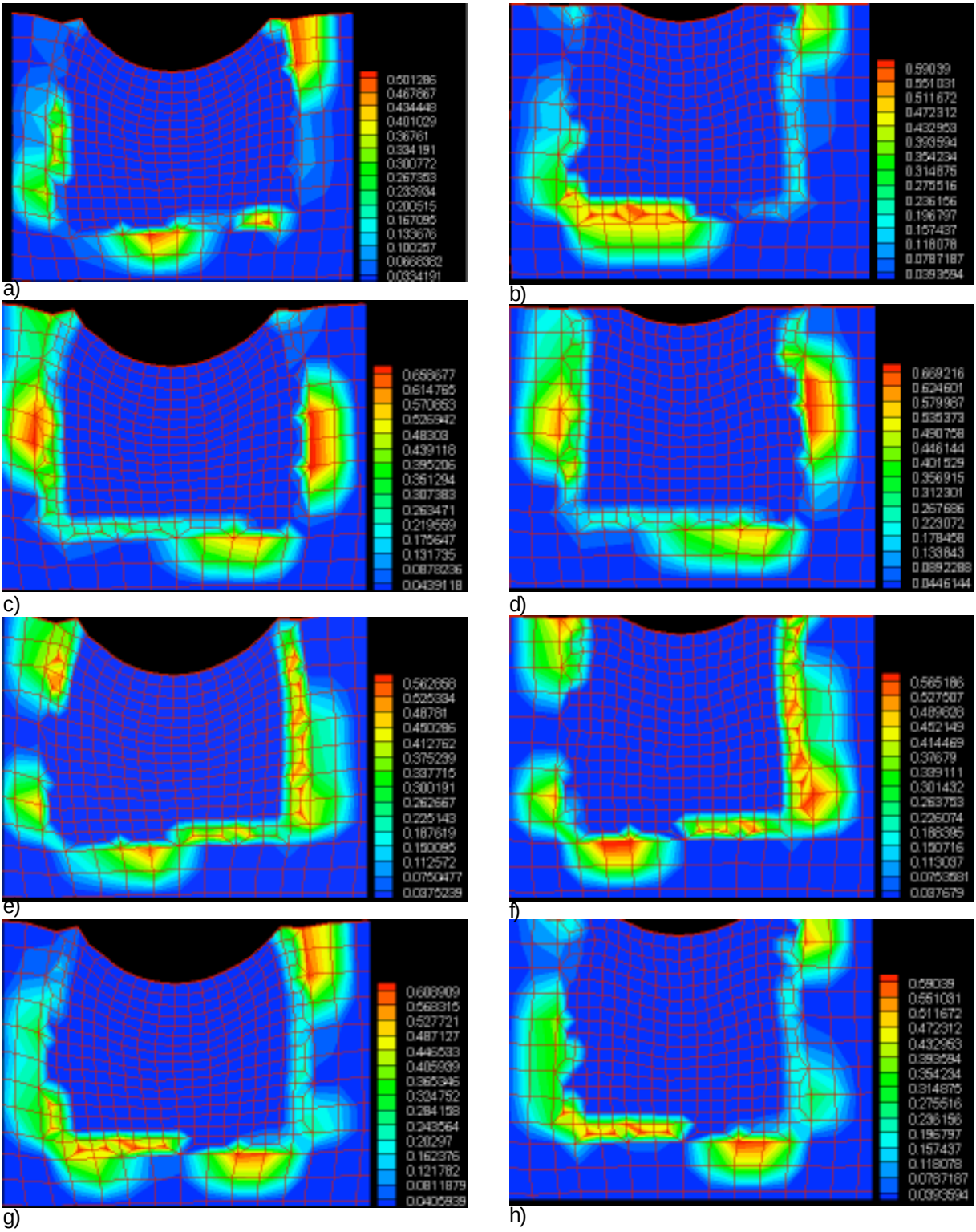

Fig 9. Transmission factor (TF) at GBs under the virtual indenter: model 1 with 9% loading.

sures are shown in Fig. 8. Near the GBs, the highest pressures are between orientations of 30° and 45°, which is near the maximum shear stress orientations of 45°. These are consistent with the observations by [28], which concluded that the GB and orientations are the principal mechanisms that can affect nanoindentation.

6.5. GB transmission factors

Fig. 9 represents the calculated transmission factors (TR) contour plots around the GBs at a normalized indentation depth of 9%, for Model 1. Plots c and d, which included the most active slip system 4 showed the highest immobile dislocation density transmission at the right hand side, which had the highest pressures. With these calculations, we determined that the hydrostatic pressures are the main factor for dislocation density activity, which is consistent with the MD observations of [36], which underscores the critical role that pressures play in dislocation emission and absorption near GBs.

7. CONCLUDING REMARKS

This study provides a predictive framework of the interrelated physical mechanisms that result in material behavior due to nanoindentation in polycrystalline aggregates with random high angle GB distributions. A multiple-slip rate-dependent crystalline constitutive formulation that is coupled to the evolution of mobile and immobile dislocation densities and a hierarchical computational scheme have been developed to investigate microstructually-induced plasticity due to the nanoindentation of f.c.c. gold aggregates. The hierarchical model was based on scaling MD displacement profiles to the microstructural scale, such that the specialize FEM can be used to track dislocation density evolution due to nanoindentation. High angle GB effects were accounted for by using random high angle misorientations for different sized aggregates and grains.

The predictions were used to determine how at local unloading, slip system activation occurs at different indentation depths. There was no significant slip system activity during the short unloading period for larger grain-size. However, similar to the random low angle GB distributions that were investigated in [29], there was significant slip system activity for smaller grain-sized models. The random high angle GBs can result in dislocation density impedance, and this results in higher accumulations of dislocation densities and plastic strains along GBs. Furthermore, it was shown how the immobile dislocation densities evolve at the maximum loading and unloading points, and how the nominal residual strains are intricately related to the accumulation of plastic strains and pressures.

We were also able to identify the exact locations and orientations of the immobile dislocation densities, plastic strains, and pressures from the indentation surface. These values generally decreased, as the normalized distance from the indenter contact point increased. At the maximum indentation point, there was a sharp increase of immobile dislocation density and plastic strains near specific GBs and surface areas. This can be due by the bending effects associated with larger indentation depth (see, for example, [3,10,11,). We used the GB interfacial scheme to determine exactly where and how immobile dislocation densities were transmitted or impeded. Our predictions indicate that the high GB transmission rates are directly related to the high pressures near the GB regions. Hence, we could relate how local pressures at specific GB locations and orientations affect immobile dislocation density evolution during nanoindentation.

The higher strength GBs had higher dislocation density evolution and higher plastic strains in comparison with the same strength GBs distributions. This is due to the stiffer GBs, which may block the transmission of dislocation densities. The calculated transmission factors for the GBs also indicate that the most active slip system at the final loading step coincided with the highest dislocation density evolution.

This study underscores how the hierarchical computational scheme, the dislocation density based formulation, and the GB interfacial kinematics can provide a comprehensive understanding of the effects of multiple-slip inelastic deformation and dislocation interactions, which are associated with nanoindenation in polycrystalline aggregates with high angle GB misorientations. Critical GB and grain locations can be identified and deformation modes can be tracked, and hence these predictions can be used to obtain desired microstructural behavior.

ACKNOWLEDGEMENTS

This work was supported from AFOSE MURI on Extreme Friction FA 9550-04-1-0381 and NSF NIRI grant 0304229.

REFERENCES

[1] Y.Y. Lim and M.M. Chaudhri // *Physica Status Solidi A* **194** (2002) 19.

[2] N. Gane and F.P. Bowden // *Journal of Applied Physics* **39** (1968) 1432.

[3] J.R. Greer and W.D. Nix // *Applied Physics a-Materials Science & Processing* **80** (2005) 1625.

[4] W.W. Gerberich, N.I. Tymiak, J.C. Grunlan, M.F. Horstemeyer and M.I. Baskes // *Journal of Applied Mechanics-Transactions of the ASME* **69** (2002) 433.

[5] J.F. Smith and S. Zheng // *Surface Engineering* **16** (2000) 143.

[6] T.A. Michalske and J.E. Houston // *Acta Materialia* **46** (1998) 391.

[7] J.D. Kiely and J.E. Houston // *Physical Review B* **57** (1998) 12588.

[8] J.D. Kiely, K.F. Jarausch, J.E. Houston and P.E. Russell // *Journal of Materials Research* **14** (1999) 2219.

[9] J.D. Schall and D.W. Brenner // *Journal of Materials Research* **19** (2004) 3172.

[10] J.A. Zimmerman, C.L. Kelchner, P.A. Klein, J.C. Hamilton and S.M. Foiles // *Physical Review Letters* **8716** (2001) 165507.

[11] J. Knap and M. Ortiz // *Physical Review Letters* **90** (2003) 226102.

[12] C.L. Kelchner, S.J. Plimpton and J.C. Hamilton // *Physical Review B* **58** (1998) 11085.

[13] A. Hasnaoui, P.M. Derlet and H. Van Swygenhoven // *Acta Materialia* **52** (2004) 2251.

[14] R.E. Miller, L.E. Shilkrot and W.A. Curtin // *Acta Materialia* **52** (2004) 271.

[15] Y. Choi, K.J. Van Vliet, J. Li and S. Suresh // *Journal of Applied Physics* **94** (2003) 6050.

[16] R. Phillips, D. Rodney, V. Shenoy, E. Tadmor and M. Ortiz // *Modelling and Simulation in Materials Science and Engineering* **7** (1999) 769.

[17] S. Suresh, T.G. Nieh and B.W. Choi // *Scripta Materialia* **41** (1999) 951.

[18] E.T. Lilleodden, J.A. Zimmerman, S.M. Foiles and W.D. Nix // *Journal of the Mechanics and Physics of Solids* **51** (2003) 901.

[19] Y. Matsukawa, K. Yasunaga, M. Komatsu and M. Kiritani // *Materials Science and Engineering a-Structural Materials Properties Microstructure and Processing* **350** (2003) 8.

[20] J.B. Ma, M.A. Zikry, W.M. Ashmawi and D.W. Brenner // *Journal of Materials Research* **22** (2007) 627.

[21] M.A. Zikry and M. Kao // *Journal of the Mechanics and Physics of Solids* **44** (1996) 1765.

[22] W.M. Ashmawi and M.A. Zikry // *Philosophical Magazine Part A* **83** (2003) 391.

[23] M.A. Zikry // *Computers & Structures* **50** (1994) 337.

[24] M.M. McCann and S.G. Corcoran, In: *Symposium on Thin Films—Stresses and Mechanical Properties*, ed. by S.G. Corcoran, Young-Chang Joo and N.R. Moody (MRS Symposium Proceedings, Pittsburgh, PA, 2003), p. U8.30.1.

[25] T. Kameda and M.A. Zikry // *International Journal of Plasticity* **14** (1998) 689.

[26] V. Randle, *The Measurement of Grain Boundary Geometry* (Bristol and Philadelphia, Institute of Physics Publishing, 1993).

[27] W. M. Ashmawi and M. A. Zikry // *Journal of Computer-Aided Materials Design* **7** (2000) 55.

[28] T. A. Ohmura, A. M. Minor, E.A. Stach and J.W. Morris, Jr. // *Journal of Materials Research* **19** (2004) 3626.

[29] J.B. Ma and M.A. Zikry // *Journal of Materials Research,* in press.

[30] W.M. Ashmawi and M.A. Zikry // *Journal of Engineering Materials and Technology-Transactions of the ASME* **124** (2002) 88.

[31] I. Baker, E. M. Schulson and J.A. Horton // *Acta Metallurgica* **35** (1987) 1533.

[32] D. J. Dingley and R. C. Pond // *Acta Metallurgica* **27** (1979) 667.

[33] T. C. Lee, I. M. Robertson and H. K. Birnbaum// *Acta Metallurgica Et Materialia* **40** (1992) 2569.

[34] F. Liu and I. Baker // *Science & Technology* **4** (1993) 416.

[35] V. Randle // *Modelling and Simulation in Materials Science and Engineering* **5** (1997) 117

[36] D. Feichtinger, P.M. Derlet and H. Van Swygenhoven // *Physical Review B* **67** (2003) 024113.